

## Nowcasting of Motion and Growth of Precipitation with Radar over a Complex Orography

L. LI AND W. SCHMID

*Atmospheric Science, Eidgenössische Technische Hochschule, Zurich, Switzerland*

J. JOSS

*Swiss Meteorological Institute, Locarno-Monti, Switzerland*

(Manuscript received 2 December 1993, in final form 1 November 1994)

### ABSTRACT

Motion vectors of radar echo patterns can be obtained by applying a cross-correlation method (e.g., the TREC method) to radar data collected several minutes apart. Here an extension of TREC, called COTREC, is presented. Based on constraints and a variational technique, this extension is an efficient objective analysis method for smoothing the motion vectors and forcing them to fulfill the continuity equation. COTREC corrects the apparently wrong vectors that are often caused by failures of TREC. This allows us to identify regions of growth and decay of radar echoes.

For different types of precipitation (convective and widespread), radar data were collected for evaluation of COTREC in complex orography. A comparison between the radial velocity components of retrieved fields of echo motion and the measured Doppler velocity has been made. A marked reduction of the differences with respect to the measured Doppler field was obtained for COTREC, as compared to TREC vectors.

A retardation of COTREC-derived motion compared to Doppler-derived motion was found in orographic precipitation. This retardation may have two causes: 1) a tendency of radar patterns to become stationary (triggered) on upsloping orography; and 2) the influence of ground clutter and shielding, also highly correlated with orography. While the first reflects the fact that propagation of echoes (by growth/decay) and translation of echoes (with the wind) are two different phenomena, the second cause is an artifact produced by the method of observation (radar) but mitigated with Doppler techniques (by suppressing the stationary ground clutter).

COTREC may be useful for nowcasting, especially in orographically complex areas: for orographic precipitation as well as for severe convective storms, the technique predicts the echo development approximately 20 min ahead, and there is good hope to extend the forecasting period.

### 1. Introduction

A number of techniques have been developed in the last three decades for extrapolation of the observed radar patterns into the future. Most of these techniques can be divided into two major groups. One group tries to find the best possible fit between two different maps of radar data that were obtained within a certain time interval (Hilst and Russo 1960). The correlation coefficient is used as an objective test criterion for the agreement between the two radar patterns. The maximum correlation coefficient determines the mean vector of displacement of the observed radar pattern that allows a linear extrapolation into the future. The technique has been refined and tested for operational applications by several authors (e.g., Bellon and Austin 1978; Browning et al. 1982). Another group of nowcasting techniques has the ability to track and forecast the areas, the mass centroids, or other parameters of closed radar contours that are assumed to represent

individual convective storms or convective cells (e.g., Barclay and Wilk 1970; Winston and Ruthi 1986). One advantage of determining motion vectors is that the growth, decay, or other variations of radar contours can be used for the extrapolation (e.g., Tsonis and Austin 1981; Schmid 1992a, b). In recent years these techniques have been further developed and applied to radar data, satellite data, or a combination of the two (e.g., Howes 1988). An overview of these techniques can be found in Collier (1989). All of these procedures do not distinguish between echo growth (especially complicated over complex orography and affecting the precipitation patterns considerably), echo translation (i.e., move with the mean wind), or propagation of echoes (i.e., apparent movement by continuously growing on one side of a precipitation cell and decaying on the other side). The latter effect means that the apparent motion deviates from the mean wind. For instance, stationary precipitation patterns may be caused by mountain ridges even when the overall wind regime would produce fast-moving precipitation patterns (e.g., Hill et al. 1981). Convective storms may propagate either to the right or the left of the mean

---

*Corresponding author address:* L. Li, Atmospheric Physics, ETH, Honggerberg HPP, CH-8093 Zurich, Switzerland.

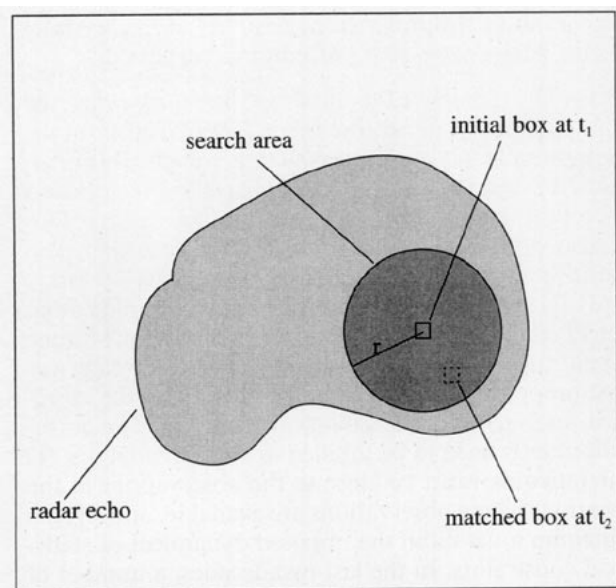


FIG. 1. Schematic illustration of the TREC method. The box at time  $t_1$  is compared to all boxes of the same size at a later time  $t_2$  that appear within a circular search area. The position of the matched box for which the correlation coefficient reaches a maximum determines the endpoint of the motion vector.

wind regime (e.g., Houze et al. 1993). For nowcasting purposes, it would be beneficial to detect the regions of precipitation growth and distinguish between propagating and translating precipitation patterns. This aim can at least partially be obtained by combining the apparent motion of precipitation with Doppler analyses.

The internal motion of small-scale radar patterns can be obtained with the TREC method (tracking radar echoes by correlation) first described by Rinehart and Garvey (1978). The method is basically the same as the correlation method mentioned above, but it is applied to small partitions of a storm system instead of to the whole storm system. A small-scale radar pattern is equivalent to a user-defined array of pixels (typically  $10 \text{ km} \times 10 \text{ km}$  in size). Such an array can well represent convex or concave indentations in the boundaries of precipitation cells on a local scale. The TREC method has originally been developed with the purpose of retrieving wind fields within radar echoes. However, TREC vectors appear to represent the airflow only in case of clear-air echoes in the planetary boundary layer (Smythe and Zrnić 1983; Tuttle and Foote 1990). In precipitation, TREC may represent the airflow at the level where the precipitation patterns are generated (Rinehart and Garvey 1978) and not necessarily at the level where the radar measurements are made. This should be considered when comparing TREC motion vectors with wind measurements.

This article presents a postprocessing of TREC vectors with a variational method that forces the constraint

of the two-dimensional continuity equation on the TREC vectors. The main motivation for the postprocessing of the TREC vectors is based on the desire to reduce the influence of “noisy” vectors, often caused by ground clutter, shielding (Tuttle and Foote 1990), and small-scale changes within the radar patterns (Rinehart 1981). Here “small-scale” refers to a box size on the order of 10 km. Such variations change the correlation between two compared boxes and, hence, increase the risk of mismatches.

The constraint of the continuity equation produces a smoothing of the TREC vectors. This, however, does not mean that reflectivity is conserved. In fact, variations of the mass of precipitation (and of the reflectivity) are to be expected. Changes of the particle distributions and related parameters are caused by growth, evaporation, and temperature changes (e.g., bright band) and produce a profile of reflectivity that strongly varies with height, as described by many authors (e.g., Joss and Pittini 1991). We want to detect echo growth and decay that may be associated with a change of intensity and/or size of translating and/or propagating radar echoes. (Note that it is not possible to separate translation and propagation with noncoherent radar only.) Considering this, we propose

- 1) to eliminate erroneous vectors from TREC, caused by clutter, shielding, and random changes of reflectivity within the radar patterns, and

- 2) to investigate growth and decay by following the development of echoes on the basis of the smoothed field of echo motion.

Section 2 of this article describes the variational technique to adjust the TREC motion vectors. The subsequent sections present analyses of real radar datasets. In section 3, the performance of the method is compared to Doppler radar data for different types of precipitation. In section 4, the potential to identify regions of echo growth and decay with the new method is investigated for both orographic precipitation and for convective storms. The remaining two sections (5 and 6) are devoted to a general discussion of the method and the conclusions.

## 2. Method

### a. TREC

Since the TREC method was well explained by Rinehart and Garvey (1978), we will only give a brief review of the principle of the method. A schematic graph of TREC is given in Fig. 1. The technique computes translation vectors of radar echo patterns that were observed twice within a short time interval  $\Delta t$ . For this, one needs to collect reflectivity data from two radar scans obtained several minutes apart. The two scans are divided into a number of equally sized boxes that are separated by a given distance. Each box of the

first scan is then compared to all possible boxes of the same size in the second scan (see Fig. 1). The correlation coefficients between the reflectivity patterns within the boxes are computed for all possible pairs of boxes, and the pair with the highest correlation coefficient is selected for the determination of the translation vector that indicates the motion of the initial box during the time period  $\Delta t$ . In most cases, it is not necessary to search the entire dataset for the best matching box. A simple way to reduce the number of pairs of boxes is to specify a circular search area around the initial box. The radius  $r$  of this area is equal to the maximum possible velocity  $V_{\max}$  multiplied with the time interval  $\Delta t$  (i.e.,  $r = V_{\max} \Delta t$ ), where  $V_{\max}$  may be determined from meteorological information or from the knowledge that one would reasonably expect in a given situation.

Important quantities of the TREC method are the box size, the grid size of the radar data, the grid size of the motion vectors, the time interval  $\Delta t$  between two compared boxes, and the lower limit of the reflectivities considered in the analysis. Rinehart (1981) gave hints for the optimal choices of these parameters. The grid size of the radar data and  $\Delta t$  determine the resolution of the  $x$  and  $y$  components of the motion vectors. For instance, a grid size of 1 km and a time interval  $\Delta t$  of 2 min mean that the  $x$  and  $y$  components of the TREC vectors reach values of . . . , 0, 8.3, 16.7 m s<sup>-1</sup>, . . . (8.3 m s<sup>-1</sup> = 1000 m/120 s). This discretisation contributes to the random errors of the TREC vectors by about 3 m s<sup>-1</sup> and can be important, depending on the overall random errors of the TREC vectors. An analysis on the optimal choice of these parameters will be given in section 5a.

The TREC vectors often show an inconsistent and noisy behavior that is mainly due to ground clutter, shielding, or failures in tracking radar echo patterns. Sophisticated methods to remove clutter echoes solve the problem only partially since the clutter echoes are often replaced by stationary echo-free "holes" or by interpolated echoes that smear the relevant finescale patterns of precipitation. Echo-free holes are considered in the TREC algorithm by assuming a low reflectivity (-90 dBZ, means "missing value") at the location of the holes. This may lead to zero-velocity TREC vectors since the large gradients in reflectivity at the boundary of the holes have a strong influence on the correlation between two compared boxes. The shielding problem in mountainous areas reduces the detection of precipitation. Failures in tracking the radar echoes in the TREC approach may arise from rapid morphological or random changes of the finescale radar patterns (Rinehart 1981).

### b. COTREC

The presented method, called COTREC (continuity of TREC vectors) is proposed to correct noisy TREC

vectors and to improve the consistency of the resulting vector field. A two-step procedure is suggested.

1) The purpose of the first step is to minimize the influence of apparently incorrect TREC vectors on the variational analysis. Vectors with zero velocity (often caused by ground clutter) are replaced by vectors that represent the average of the neighboring vectors. This is also done for vectors that deviate more than 25° from the mean direction of the neighboring vectors.

2) The second step uses a variational technique that forces continuity on the TREC-derived motion vectors. Application of variational methods to meteorology was first proposed by Sasaki (1958, 1970a,b) for the objective analysis of meteorological data. Two basic requirements need to be fulfilled in such an analysis: (i) the outcome must be close to the observations at the locations where observations are available, and (ii) the outcome must fulfill the imposed dynamical or statistical constraints. In the last two decades, a number of variational techniques have been developed and widely applied to meteorological fields (e.g., Navon and David 1987). The continuity equation, forcing measured wind fields to zero divergence over the measuring domain, is one of the often-used constraints (e.g., Sherman 1978).

The classical solution of a variational analysis can be expressed in terms of minimizing a cost function  $J$ ,

$$J(u, v) = \int_{\Sigma} [(u - u^0)^2 + (v - v^0)^2] dx dy, \quad (1)$$

in such a way that a given constraint is fulfilled. The constraint of the two-dimensional Boussineq mass continuity equation

$$\frac{\partial u}{\partial x} + \frac{\partial v}{\partial y} = 0 \quad (2)$$

is considered here. The  $x$  and  $y$  components of the observed motion vectors (the TREC vectors here) are  $u^0(x, y)$  and  $v^0(x, y)$ , whereas the components  $u(x, y)$  and  $v(x, y)$  are the solution of the variational analysis. The symbol  $\Sigma$  in Eq. (1) stands for the motion vector domain. It can be shown (see Bertsekas 1982) that the problem of determining the stationary points of  $J(u, v)$  [Eq. (1)] under the constraint Eq. (2) is equivalent to the problem of determining the stationary points of the following scalar function with respect to the three variables  $u, v, \lambda$ :

$$F(u, v, \lambda) = \int_{\Sigma} \left[ (u - u^0)^2 + (v - v^0)^2 + \lambda \left( \frac{\partial u}{\partial x} + \frac{\partial v}{\partial y} \right) \right] dx dy, \quad (3)$$

where  $\lambda(x, y)$  is usually denoted as the Lagrangian multiplier. Thus, the minimization of the cost function

$J$  [Eq. (1)] subject to the constraint of Eq. (2) is replaced by an unconstrained minimization of  $F(u, v, \lambda)$ . In this way, the "strong constraint" minimization (Sasaki 1970a) is performed, which means that the condition [Eq. (2)] is satisfied exactly in the variational analysis.

The associated Euler–Lagrange equations whose solution minimizes  $F$  are

$$u = u^0 + \frac{1}{2} \frac{\partial \lambda}{\partial x} \quad (4)$$

$$v = v^0 + \frac{1}{2} \frac{\partial \lambda}{\partial y} \quad (5)$$

$$\frac{\partial u}{\partial x} + \frac{\partial v}{\partial y} = 0 \quad [\text{Eq. (2)}]$$

$$\lambda(x, y) = 0 \quad (6)$$

along the boundary  $\Gamma$  of  $\Sigma$ .

Differentiating Eqs. (4) and (5) and substituting them into Eq. (2) yields

$$\frac{\partial^2 \lambda}{\partial x^2} + \frac{\partial^2 \lambda}{\partial y^2} = -2 \left( \frac{\partial u^0}{\partial x} + \frac{\partial v^0}{\partial y} \right). \quad (7)$$

This is a partial differential equation of elliptic type. The given boundary condition [Eq. (6)] means that the airflow is allowed to pass freely through the boundary (Sherman 1978).

Equation (7) can be expressed in a finite-difference form at every interior grid point  $(i, j)$  for computational purposes:

$$\frac{\lambda_{i+1,j} - 2\lambda_{ij} + \lambda_{i-1,j}}{(\Delta x)^2} + \frac{\lambda_{i,j+1} - 2\lambda_{ij} + \lambda_{i,j-1}}{(\Delta y)^2} = -2\epsilon_0, \quad (8)$$

where  $\epsilon_0 = (u_{i+1,j}^0 + u_{i-1,j}^0)(2\Delta x)^{-1} + (v_{i,j+1}^0 + v_{i,j-1}^0) \times (2\Delta y)^{-1}$ . The parameters  $\Delta x$  and  $\Delta y$  mark the grid spacing. The adjusted motion vectors are then obtained using the following difference formulation of Eqs. (4) and (5):

$$u_{i,j} = \frac{1}{4} (u_{i+1,j}^0 + 2u_{ij}^0 + u_{i-1,j}^0) + \frac{1}{2} \left( \frac{\lambda_{i+1,j} - \lambda_{i-1,j}}{2\Delta x} \right) \quad (9)$$

$$v_{i,j} = \frac{1}{4} (v_{i,j+1}^0 + 2v_{ij}^0 + v_{i,j-1}^0) + \frac{1}{2} \left( \frac{\lambda_{i,j+1} - \lambda_{i,j-1}}{2\Delta y} \right). \quad (10)$$

Equation (8) can be solved using either an iterative method (i.e., the SOR—successive over relaxation approach, Press et al. 1991) or the FTM (Fourier transfer method). The SOR method gives a faster convergence to the solution than the traditional Gauss–Siedel method. The FTM is suitable for boundary value problems of partial differential equations, especially for periodic boundary conditions.

### c. Echo growth and decay

The lack of information on the growth and decay patterns of radar echoes is one major source of poor nowcasting of precipitation systems (Browning et al. 1982). It is also evident that complex orography affects these patterns in a significant manner. An objective identification of these patterns would be a great help for nowcasting purposes and also for research topics that are related to the apparent links between orography and precipitation. The internal motion vectors of radar patterns provide the basis for the quantitative identification of small-scale development and dissipation of radar echo patterns over the period of echo tracking. The method to obtain the patterns of echo growth and decay is straightforward: one calculates the difference in mean radar reflectivity between a box of the second scan and the corresponding box of the first scan. The location of the box of the second scan is determined by the given field of the COTREC vectors. This procedure is repeated for each box of the first scan. Areas of positive values for the calculated difference represent regions of echo growth, while areas of negative values indicate regions of echo decay.

## 3. Performance

### a. Characteristics of the radar and the data

In this section we compare TREC and COTREC motion vectors with velocity measurements obtained from a Doppler radar. The Doppler measurements are used to evaluate the agreement between the (CO)TREC vectors and Doppler velocity. The field of the COTREC vectors should be closer to the Doppler wind field than the field of the original TREC vectors if COTREC can effectively correct erroneous TREC vectors.

The data for this comparison are taken from a Doppler weather radar that is located at the ETH in Zurich, Switzerland. The main characteristics of the radar are given in Table 1. The resolution of the archived data is 300 m in range and 1° in azimuth. The data were transformed into a Cartesian coordinate sys-

TABLE 1. Main characteristics of the ETH Doppler radar.

Frequency	5.66 GHz
Peak power output	250 kW
Pulse length	0.5 and 3 $\mu$ s
PRF	250–1200 Hz
Velocity unfolding	Dual PRF mode (1200/800 Hz)
Antenna beamwidth	1.6° circular
Polarization	Linear horizontal
Transmitter	Magnetron type
Receiver: reflectivity channel	Logarithmic
Doppler channel	Linear with STALO and COHO
Doppler filters	14 IIR* with varying stopband and passband

\* IIR—infinite impulse response.

tem of  $1 \text{ km} \times 1 \text{ km}$  grid size. Ground clutter echoes were eliminated by using the "pulse pair" technique originally described by Passarelli (1981). A clutter-to-signal ratio was computed for each pixel, and pixels with values larger than 5 dB were removed. This results in clutter echoes being replaced by echo-free holes. The good behavior of this algorithm is described and compared to alternative algorithms in Schmid et al. (1991), which also gives more details of the radar, the data, and the evaluation programs.

The precipitation event was caused by a cold front that passed within radar range during the night of 15/16 June 1991. This event has been selected since it produced both widespread and convective precipitation patterns simultaneously. This provides a good opportunity to evaluate the efficiency of COTREC for different radar patterns. The wind direction was mainly from the southwest, and the Doppler radar detected radial velocities up to about  $25 \text{ m s}^{-1}$ . The sounding data from 0000 UTC 16 June 1991 (Payenne sounding, located about 100 km southwest of the ETH radar) yielded a fairly uniform wind profile between 850 hPa (mean altitude of the radar measurements) and 500 hPa (mean altitude at which the precipitation patterns are thought to be generated);  $230^\circ/20 \text{ m s}^{-1}$  and  $250^\circ/25 \text{ m s}^{-1}$  were recorded at these altitudes. Figure 2a shows the fields of radar reflectivity taken from a  $0.5^\circ$  PPI (plan position indicator) scan obtained at 2310 UTC. Radar echoes of widespread precipitation are mainly found in the range 20–120 km northeast of the radar, whereas convective cells of moderate intensity appeared in the north (90 km away), east (50 km away), and southwest to west from the radar site.

The radar data collected at 2310 and 2312 UTC were analyzed using a box size of 10 km and a grid size of 6 km for the retrieved motion vectors. These values are well within the range recommended by Rinehart (1981) for optimal application of TREC. A sensitivity analysis of these parameters is given in section 5a. The lower boundary of the reflectivities considered is set to 10 dBZ. The resulting field of the TREC vectors is presented in Fig. 2c. These vectors show a considerable small-scale variability overlaid on the overall flow pattern from southwest to northeast. At least some of these vectors are incorrect, considering the continuity of the motion field. Examples are the zero velocity vectors located 50 km north of the radar or those vectors pointing toward the opposite direction than the neighboring vectors (see, e.g., the vectors at the locations 50/20 km or 20/100 km east/north of the radar, where 50/20 km east/north means 50 km east and 20 km north of the radar). These vectors reflect failures of TREC mainly caused by ground clutter (see Fig. 2b). Application of COTREC eliminates these incorrect vectors and causes a considerable smoothing of the motion field (see Fig. 2d).

### b. Comparison with Doppler velocities

The procedure to assess the agreement of TREC and COTREC vectors to Doppler measurements is basically the same as applied to clear-air echoes by Tuttle and Foote (1990). These authors argued that the retrieved motion vectors should represent the horizontal winds within the clear-air radar echoes if agreement exists between  $V_R$  (the radial component of the retrieved motion vectors) and  $V_D$  (the arithmetic average of the measured Doppler velocities within a box). In precipitation (causing propagating radar echoes) we still expect a reduction of the scatter between  $V_R$  and  $V_D$  when COTREC is able to correct erroneous TREC vectors. A scatterplot of  $V_R$  versus  $V_D$  of TREC is given in Fig. 2e. It is evident that the scatter around the regression line is large. The RRMS error (residual root-mean-square) of this scatter is  $10.6 \text{ m s}^{-1}$ .

The scatter of the points is especially large in that part of the figure where the Doppler velocities are positive (RRMS =  $12.6 \text{ m s}^{-1}$ ). This part contains the region of widespread precipitation (see Fig. 2a), whereas the negative Doppler velocities are found in convective precipitation with more distinct radar echoes being easily tracked. There one finds a RRMS error of  $5.9 \text{ m s}^{-1}$ .

A scatterplot of  $V_R$  versus  $V_D$  based on the COTREC vectors (shown in Fig. 2d) is given in Fig. 2f. A comparison with Fig. 2e shows that the scatter of the points about the regression line has decreased dramatically. The correlation coefficient between the two quantities ( $V_R$  and  $V_D$ ) increases from 0.79 (TREC) to 0.97 (COTREC), and the RRMS error of the differences  $V_R - V_D$  is reduced from 10.6 to  $3.6 \text{ m s}^{-1}$ . The remaining RRMS error is nearly the same for both regimes of precipitation: in widespread precipitation in the northeast for positive Doppler velocities ( $3.7 \text{ m s}^{-1}$ ), as well as for the negative ones in the convective part in the southwest ( $3.3 \text{ m s}^{-1}$ ). This shows the excellent performance of COTREC to reduce the RRMS error in both regimes of precipitation.

A visual comparison of the shaded patterns of Doppler velocity and of the radial component of the retrieved motion vectors yields another way to assess the reliability of COTREC (see Fig. 3). The two patterns differ by less than one level ( $6.4 \text{ m s}^{-1}$  in velocity) at almost all locations. The COTREC velocities are somewhat larger than the Doppler velocities. This finding is consistent to Fig. 2f, which shows that the slope of the regression line between the COTREC and the Doppler velocities is about 3% larger than one. This finding might reflect the fact that the wind speed is slightly increasing between the altitude of the radar measurements and the altitude of precipitation generation aloft.

### c. Clutter and shielding

Radar observations of precipitation are often disturbed by clutter echoes (ground targets) and by

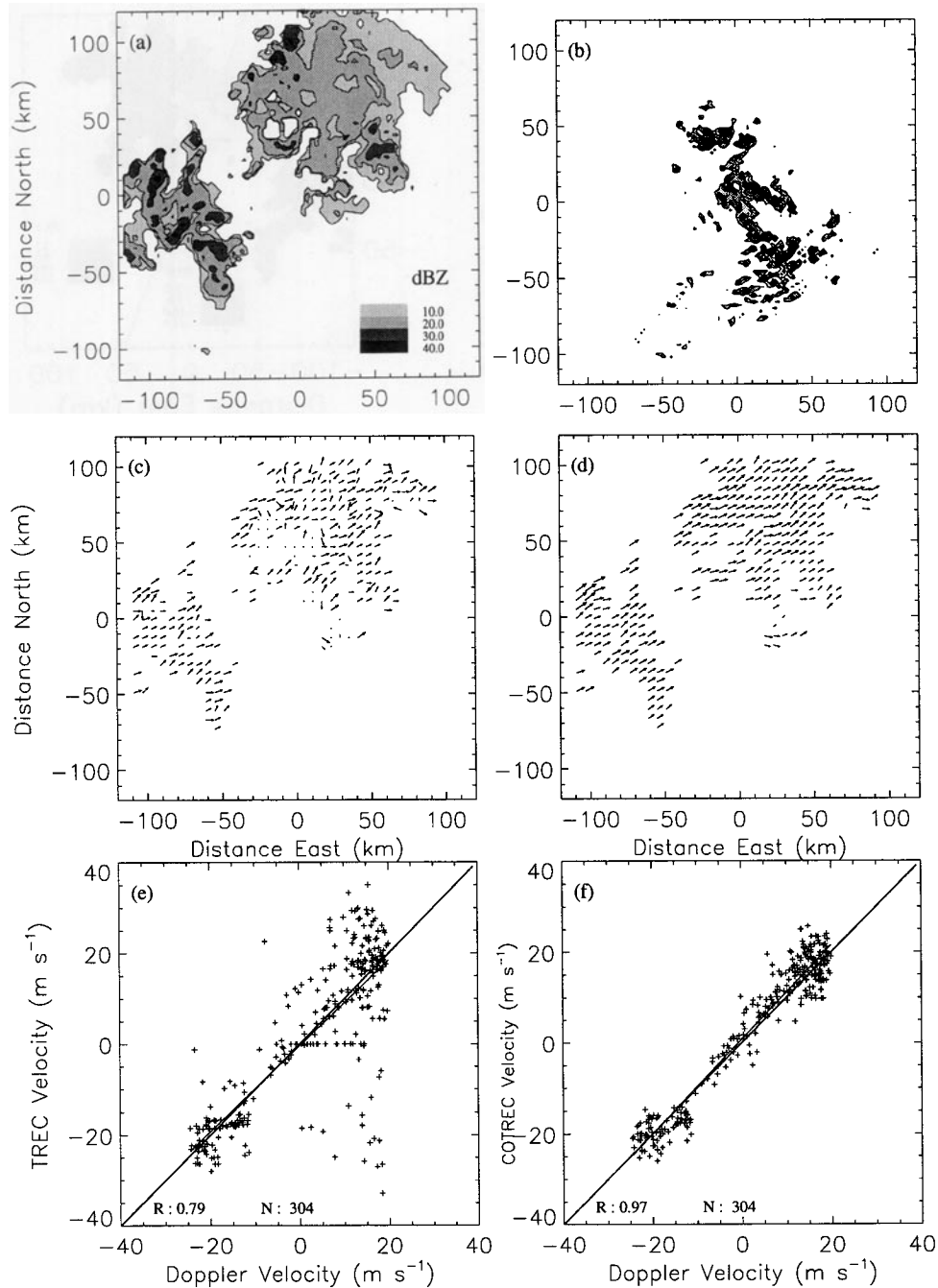


FIG. 2. (a) PPI reflectivity (measured with the ETH Doppler radar at an elevation angle of  $0.5^\circ$ ) at 2310 UTC 16 June 1991. (b) The PPI reflectivity of ground clutter, measured with the ETH-radar at an elevation angle of  $0.5^\circ$  during fair weather. The shading of the reflectivity levels is the same as in (c). (d) The TREC vectors and the COTREC vectors retrieved from the PPI reflectivity data collected at 2310 and 2312 UTC 16 June 1991. The maximum magnitude of the plotted vectors is  $33 \text{ m s}^{-1}$ . (e), (f) A scatterplot of Doppler velocity versus the radial components of the TREC vectors (e) and the COTREC vectors (f), respectively. The 1:1 line, the regression line, the correlation coefficient  $R$  between the compared quantities and the number of the retrieved vectors  $N$  are also given in the two diagrams.

shielding effects. The TREC technique is sensitive to both (Tuttle and Foote 1990). Clutter echoes are stationary and lead to signatures of high correlation and,

hence, to TREC vectors of zero magnitude. Tuttle and Foote introduced simulated ground targets in a measured radar field of precipitation and found that even

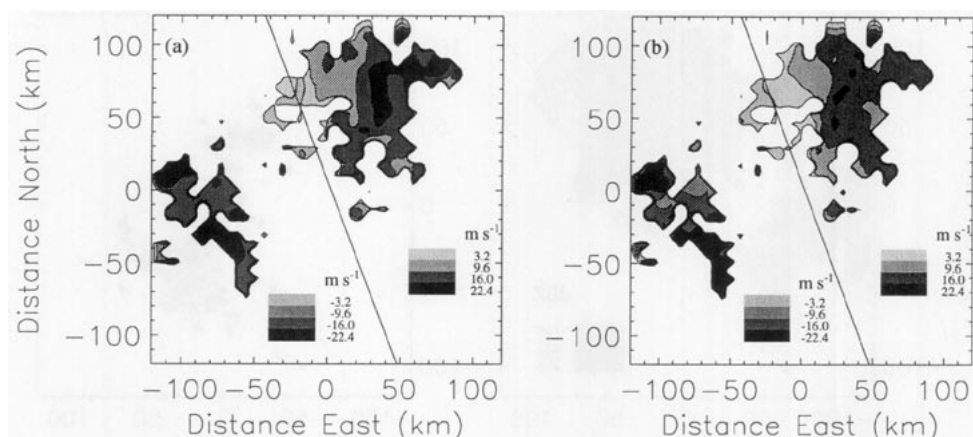


FIG. 3. (a) The radial component of the COTREC velocities. (b) Doppler velocities at 2310 UTC 16 June 1991. The solid lines separate the regions with a motion towards the radar (left side) and away from the radar (right side). Note that the mesh size of the Doppler data has been adapted to the mesh size of the COTREC data.

small clutter echoes (approximately 1-km radius) can influence TREC significantly. The clutter problem is especially significant in mountainous areas, for example, at the northern border of the Swiss Alps (Joss and Waldvogel 1990). Figure 2b shows the ground clutter echoes of the ETH radar during fair weather. Doppler suppression algorithms (Schmid et al. 1991) have been used to remove most of the ground clutter during radar data collection on 16 June 1991. The clutter echoes are replaced by echo-free holes that remain stationary, cause zero TREC vectors (see, e.g., Figs. 2a and 2c at the position 10/45 km west/north of the radar), and appear in the scatter diagram of Fig. 2e as a horizontal line of data points.

To minimize the influence of clutter on the motion vectors, zero velocity vectors can be omitted before applying a variational technique to the data. This method has similar performance as the correlation thresholding method used by Tuttle and Foote (1990) in which they removed all vectors for which the correlation is larger than a specific threshold. Both methods risk to throw away reliable vectors. This risk can be reduced by replacing apparently “bad” vectors by an average of the surrounding vectors. This is done in COTREC; see section 2b. Most zero velocity vectors have been replaced by more consistent vectors before applying the variational technique to the data. The risk, however, remains for COTREC vectors to be somewhat biased toward smaller values of velocity (e.g., 50 km north of the radar).

Shielding by mountains leads to “blind” areas, where the radar will not (or only partially) detect precipitation. A complete shielding of the radar beam causes similar effects on the TREC vectors as clutter echoes. A partial shielding, however, conserves to some degree the small-scale radar patterns, and, hence, the resulting TREC and COTREC vectors. The patterns of echo

growth and decay are affected by shielding even when the COTREC vectors are reliable. This point will be considered in the next section, presenting the radar patterns of echo growth and decay in various precipitation situations.

#### 4. Motion, growth, and decay in complex orography

##### a. Orographic precipitation

Precipitation patterns are affected by topography. Orographic rainfall enhancement can be attributed, for instance, to the “seeder–feeder” mechanism described by Bergeron (1965). Precipitation particles falling from upper-level “seeder” clouds collect small droplets within low-level “feeder” clouds that are mainly formed over the tops of hills. The analysis of radar and rain gauge data in southern Wales has shown that the generation of orographic rain is consistent with the seeder–feeder mechanism (Hill et al. 1981). The largest enhancement of rainfall occurred in cases with strong winds and high relative humidity in the lowest 2 km above the ground. The radar observations revealed that over 80% of the rainfall enhancement occurred in the lowest 1.5 km above a hill.

Local orography can also initiate, support, or suppress deep convection. Many flood events are known to be caused by a sequence of convective cells that are formed on the upwind side of a mountain ridge (e.g., Chen et al. 1991). The factors determining the exact location of cell formation are complex and can usually only be identified by a combined analysis of synoptic and mesoscale ground network and radar data and with the help of proper model simulations (e.g., Watanabe and Ogura 1987). A real-time identification of orographic growth of radar echo patterns is useful for nowcasting purposes and contributes to forecasts of flood events.

In this section we analyze a precipitation event with embedded convection from 11 March 1992. This event was observed within the project "Winterregen," whose main purpose is to investigate the wet deposition of air pollutants in wintertime precipitation situations (Staehelin et al. 1993). Meteorological, microphysical, and chemical data of this case were collected along the slope of the "Rigi" Mountain, 40 km south of the radar site (see Fig. 4). The precipitation was caused by a cold front that passed over Switzerland within a westerly wind field (approximately  $20 \text{ m s}^{-1}$ ) in the free atmosphere. The temperature at the Rigi Mountain (1620 m MSL) dropped from  $3^{\circ}$  to  $0^{\circ}\text{C}$  between 0130 and 0230 UTC. Widespread precipitation with embedded convection was mainly observed in the hours after the frontal passage at the ground.

Doppler radar data were collected at 10-min intervals. PPI scans at an elevation angle of  $1.5^{\circ}$ , sector volume scans, and RHI scans toward the Rigi Mountain were made. The time interval between two consecutive PPI scans was lowered to 2 min at specific periods. Here we will concentrate on the time period between 0230 and 0330 UTC. Graupel showers were observed during that time on the Rigi Mountain. The RHI sections and the data from a second, vertically pointing Doppler radar (located about 3.5 km to the west of the Rigi Mountain) confirmed the convective character of precipitation and the lack of a bright band at that time period (Mosimann 1994). This means that "brightband" effects on the growth and decay of radar echoes can be neglected here, even though the radar

measured close to the level of  $0^{\circ}\text{C}$  temperature in some areas.

Figure 5 shows the radar reflectivity at 0300 (Fig. 5a) and 0310 UTC (Fig. 5b). These patterns suggest that the most intense precipitation is mainly located along the foothills at the northern border of the Swiss Alps (compare Figs. 5a and 5b to Fig. 4). The COTREC method was applied to the PPI scans taken at 0300 and 0302 UTC. A box size of 16 km and a grid spacing of 10 km was selected, and the lower boundary of the reflectivities considered was set to 10 dBZ. Figure 5c shows the resulting motion vectors and the areas of echo growth (solid contours) and decay (dashed contours) in units of decibels per minute. Echo growth is indicated at two locations: 1) within an elongated area that is located northwest of the two prealpine mountains Rigi and Pilatus, and 2) at about 50 km west-northwest of the radar site. Several regions of echo decay are found more toward the north, east, and south of the radar site.

It should be noted that these areas of echo growth and decay are based on a time interval of 2 min. The question arises if these areas also indicate echo growth and decay on a larger timescale (e.g., 10 min). A comparison of Figs. 5a and 5b suggests a positive answer to this question. For instance, the two precipitation bands located south-southwest and 40–50 km west-northwest of the radar site are apparently growing, whereas the radar echoes in the north and east of the radar site are decaying. In general, one finds an excellent agreement between the growth or decay patterns

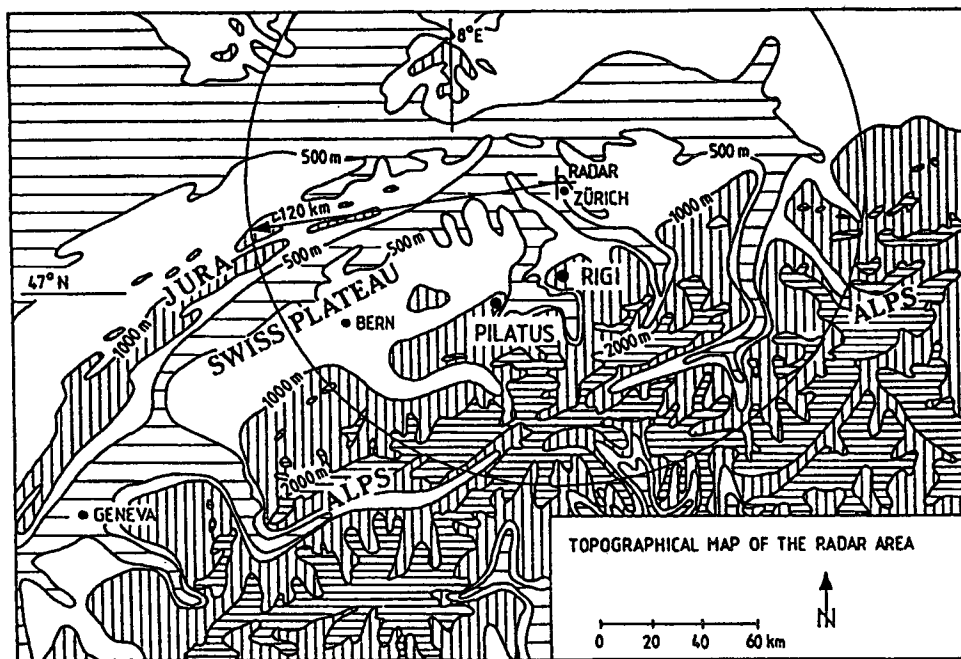


FIG. 4. Topographical map of the radar range (bounded by the solid circle) and neighboring regions. The locations of the Rigi and Pilatus Mountains are also indicated in the figure.



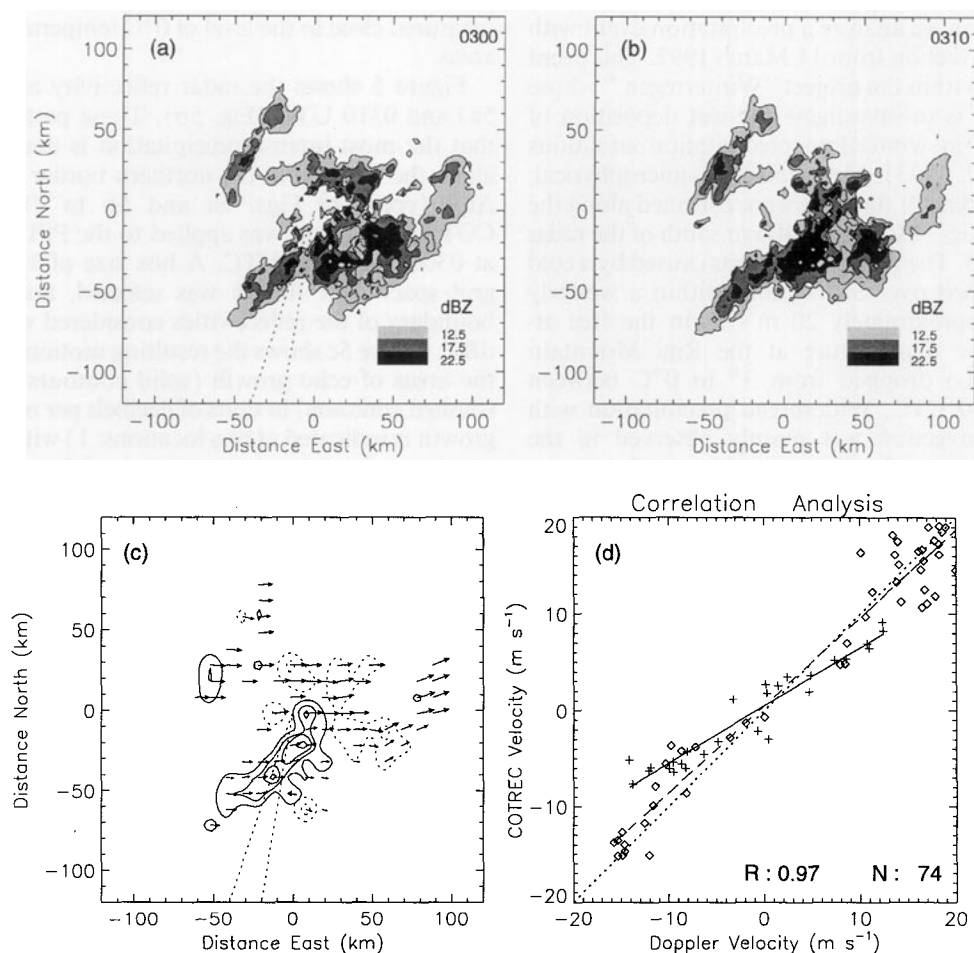


FIG. 5. (a), (b) The shaded patterns of PPI reflectivity taken at an elevation angle of  $1.5^\circ$  at 0300 and 0310 UTC 11 March 1992. (c) The COTREC vectors and the areas of echo growth (solid lines) and echo decay (dashed lines), computed from the PPI scans available at 0300 and 0302 UTC. The maximum magnitude of the plotted vectors is  $20 \text{ m s}^{-1}$ . The contour lines start at  $0.1 \text{ dB min}^{-1}$  and continue in steps of  $0.2 \text{ dB min}^{-1}$ . (d) Scatterplot of Doppler velocities versus the radial components of the COTREC velocities. The crosses and the solid regression line represent the measurements between 10 and 70 km south of the radar site. The squares and the dashed regression line represent the data between 10 km south and 80 km north of the radar. The dotted line is the 1:1 line. The straight dotted lines in (a) and (c) bound the sector of shielding caused by the "Uetliberg" Mountain close to the radar site.

obtained with COTREC and the trends seen when comparing Figs. 5a and 5b.

The same procedure for determining growth and decay of radar echoes was repeated for the period of 0230–0330 UTC. These patterns were fairly stationary during this period, leading to a time average showing significant echo growth and decay (see Fig. 6a). The major centers of growth are found on the upwind flank of mountain ridges (compare Figs. 4, 5c, and 6). A plot of the accumulated rainfall rate (retrieved from the radar data) is given in Fig. 6b. The major centers of rainfall intensity are located downwind of the centers of echo growth (compare Figs. 6a and 6b). These results support an orographic impact on the associated precipitation patterns and confirm the apparent link be-

tween orography and the growth of embedded convective cells in this precipitation event. For nowcasting, it would be important to realize that the main centers of echo growth remain stationary. This information can be obtained from subsequent radar images and used for a forecast of echo growth that is valid as long as the orographic impact on precipitation remains active.

The influence of clutter and shielding on COTREC velocities can be seen in Fig. 5c. Clutter affects the patterns of precipitation mainly in the south and southeast of the radar. The Uetliberg Mountain, located 6.5 km south-southwest of the radar, causes a significant (but not complete) shielding in the sector indicated by two straight dashed lines in Figs. 5a and 5c.

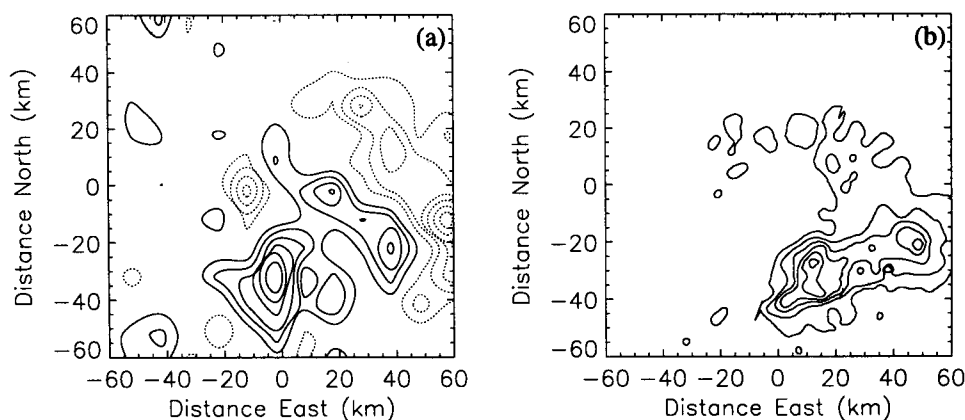


FIG. 6. (a) Areal distribution of the echo growth and decay within a range of 60 km around the ETH radar. The result is an average of the growth and decay patterns (calculated from COTREC) from 0230 to 0330 UTC. Contour values start at  $0.5 \text{ dB min}^{-1}$  and continue in increments of  $0.5 \text{ dB min}^{-1}$ . The solid lines indicate echo growth and the dashed lines indicate echo decay. (b) The accumulated rainfall (mm) for the same period, computed from the radar data. The contours start at 0.5 mm and continue in increments of 0.3 mm.

The shielding effect on the reflectivity patterns can be seen in Figs. 5a and 5b. The horizontal gradients of reflectivity along the boundaries of the shielded range are stationary and, together with the clutter echoes, decrease the COTREC-detected velocities. This is confirmed when the COTREC vectors given in Fig. 5c are compared to the Doppler velocities. The northern part of the radar range (with a small influence of clutter and shielding) shows a fairly homogeneous westerly motion of about  $15 \text{ m s}^{-1}$ . The velocity of the radar patterns is considerably smaller in the southern part of the radar range where clutter and shielding are more extended than in the northern part. This difference in velocity is not supported by the Doppler velocities, as shown by the scatterplot of Fig. 5d. The data in this figure were divided into two groups, and regression lines were calculated for each group separately. The crosses and the solid regression line represent all vectors that are observed 10–70 km south of the radar site, whereas the squares and the dashed regression line represent all other vectors. The dashed regression line (representing nearly clutter-free areas) is close to the  $45^\circ$  line (dotted in Fig. 5), but the solid regression line, representing the areas affected by clutter and shielding, confirms that the COTREC vectors are biased low when clutter and shielding are significant. This retardation effect may also be caused by precipitation that is continuously triggered on upsloping mountain flanks. This bias affects the patterns of growth and decay to a minor degree only in this case since the effective displacement of the radar patterns within the time lag considered (2 min) is small (on the order of 1–2 km) compared to the size of the areas of echo growth and decay (typically  $20 \text{ km} \times 20 \text{ km}$ ; see Fig. 5).

#### b. Severe convective storms

The main purpose of this section is to investigate the potential of COTREC-detected patterns of echo growth and decay for nowcasting severe convective storms. A rather complex evolution (21 July 1992) of a severe storm has been selected for this analysis. This storm caused the most extended hail damages in Switzerland since 1971. Further analyses of this case are underway. PPI scans were made in time steps of 2 and 10 min, and RHI and sector volume scans were obtained at 5-min intervals. Here the time period between 1540 and 1620 UTC is investigated, when several isolated cells began to form a mesoscale convective complex.

The evolution of the storm is illustrated in Figs. 7a–d, which show the patterns of radar reflectivity in time intervals of 10 and 20 min, respectively. Isolated cells moved into the radar range from southwestern direction or developed within the radar range. Later some of these cells began to merge and form a squall line that continued to propagate toward northeastern direction at an average speed of  $20 \text{ m s}^{-1}$ . Peak intensities of more than 60 dBZ were observed. The motion vectors based on COTREC and the areal distribution of echo growth and echo decay at 1540 and 1620 UTC are given in Figs. 7e and 7f. Each figure is based on pairs of PPIs that were obtained at 1540, 1542 and 1620, and 1622 UTC, respectively. The radar patterns are only drawn at locations where the radar reflectivity is greater than 20 dBZ. This boundary has been selected because the reflectivities in the range 10–20 dBZ are affected by clear-air echoes from insects and by second-trip echoes [for definition of second-trip echoes see, e.g., Rinehart (1991)]. Six centers of echo growth and echo decay and the corresponding radar features are

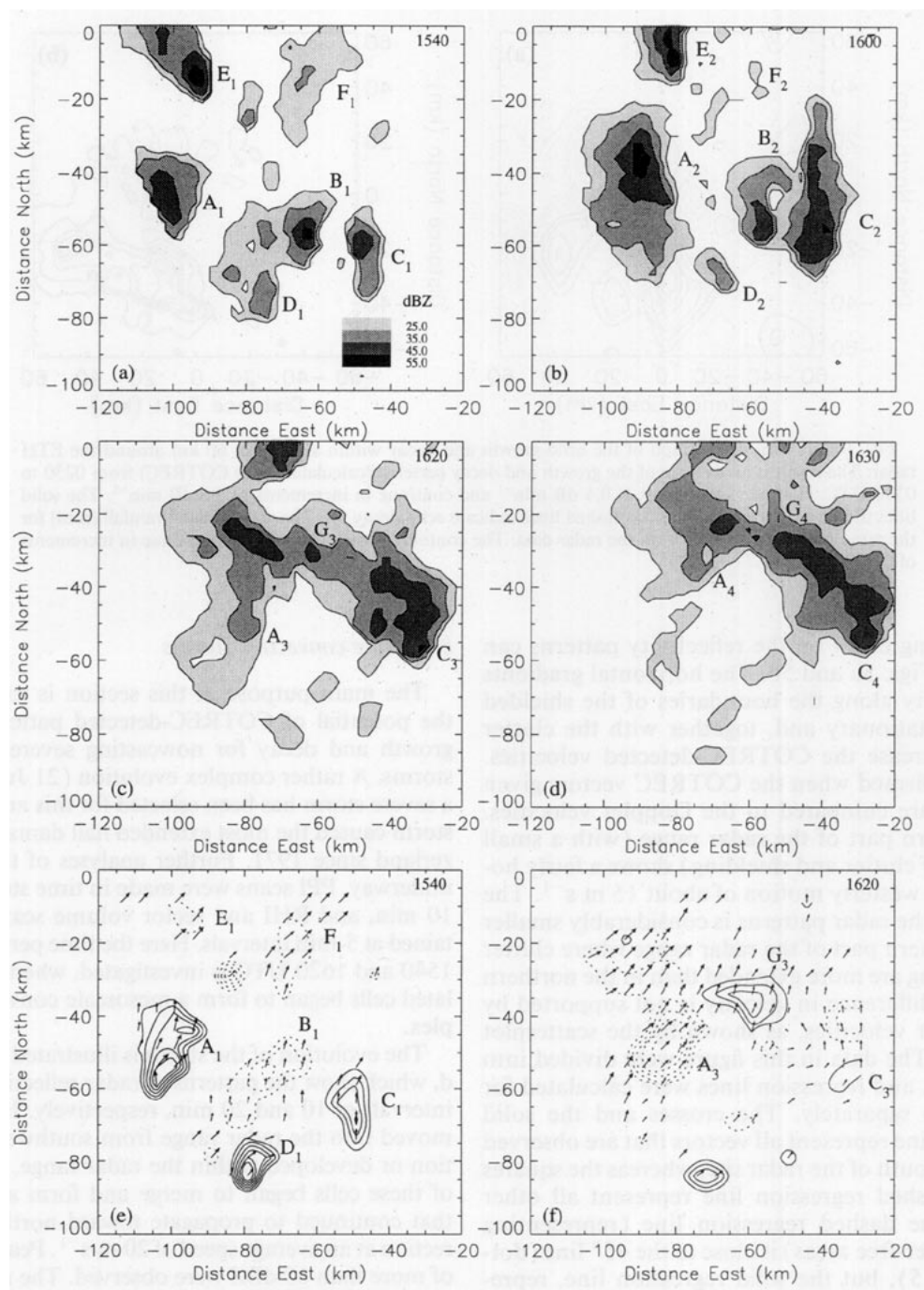


FIG. 7. (a)–(d) The shaded patterns of PPI reflectivity at 1540, 1600, 1620, and 1630 UTC, for the storm from 21 July 1992. The elevation angle is  $1.5^\circ$ . The reflectivity values start at 20 dBZ and are plotted in increments of 10 dB. (e), (f) Same as Fig. 5c, except that the contour lines start at  $0.25 \text{ dB min}^{-1}$  and continue in increments of  $0.25 \text{ dB min}^{-1}$ .

denoted with labels A–F in Figs. 7a and 7e. The corresponding features at different times are marked with different subscript labels.

An answer to the question of how well the COTREC-detected areas of echo growth and decay can predict the future behavior of the corresponding radar patterns

can be found by comparing the intensity and size of the labeled radar features at different times. For instance, feature  $B_1$  is collocated to a center of echo decay at 1540 UTC (compare Figs. 7a and 7e). This collocation would imply a subsequent weakening of feature  $B_1$ . A visual comparison of Figs. 7a and 7b confirms

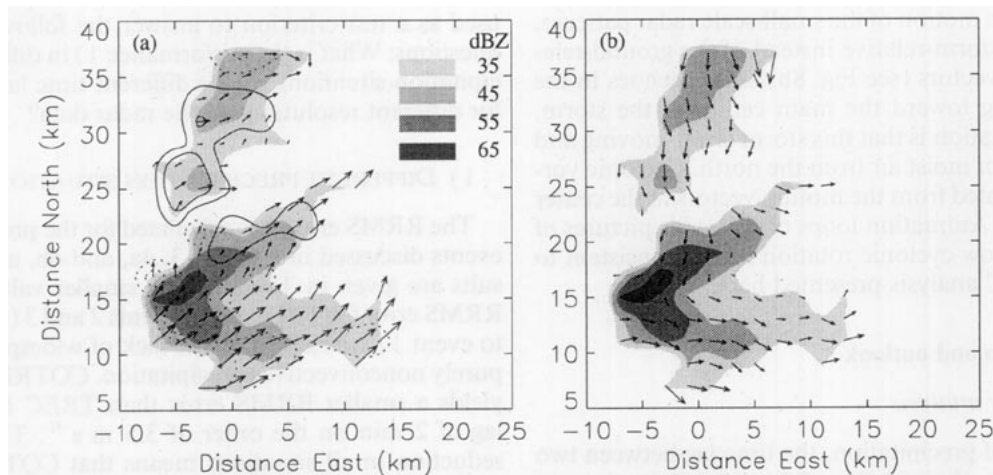


FIG. 8. (a) The COTREC vectors superimposed on the reflectivity patterns of a severe hailstorm from 15 July 1982. The PPI data were collected at 1413 and 1415 UTC. The box size and the spacing between neighboring vectors are 4 and 2 km, respectively. The motion vectors are relative to the ground. The solid (dashed) contour lines, starting at  $0.5 \text{ dB min}^{-1}$  and continuing in increments of  $0.5 \text{ dB min}^{-1}$ , show the growth (decay) regions within the radar echo patterns. (b) Same as in (a) except that the motion vectors are relative to the mean storm motion. The average movement of the storm is  $6.0 \text{ m s}^{-1}$  in speed and  $200^\circ$  in azimuth (toward the north-northeast direction).

this expectation: feature  $B_2$  is apparently weaker than feature  $B_1$ . Examples of growing features during the period 1540–1600 UTC are features  $A$  and  $C$  (compare Figs. 7a and 7b). Both features are collocated to centers of echo growth (compare Figs. 7a and e). In case of feature  $A_1$ , one can attribute part of the echo “growth” to the fact that the feature entered the range of radar data collection (120 km). Features  $D$  and  $E$  are examples that do not confirm the prediction of the COTREC-detected growth and decay areas. Feature  $D_1$  should grow but did not. In fact, we found that this feature grew from 1540 to 1550 UTC but began to decay soon after 1550 UTC (not shown here). This feature was apparently short-lived. The opposite behavior was found in case of feature  $E$ . This feature remained strong, although it was attributed to a small area of echo decay at 1540 UTC. At 1620 UTC, one can identify two regions of major echo growth and echo decay ( $G_3$  and  $A_3$ , see Fig. 7f). Both regions predict correctly the intensity of the corresponding radar patterns seen 10 min later (compare Figs. 7c and 7d). In case of feature  $C_3$ , one finds two neighboring regions of echo growth and echo decay at 1620 UTC. The feature weakened a bit 10 min later, which is partly consistent with the distribution of echo growth and decay seen in Fig. 7f.

In summary, nine features have been considered, and a growth/decay of these features was correctly predicted in six cases. Evaluating the nine features quantitatively (for details see Li 1994) yields a correlation coefficient of 0.57 between the observed growth/decay (based on the 10/20-min intervals) and the predicted growth/decay (based on the 2-min interval). Such a correlation is not very high but it is significantly

different from zero at the 10% level, thus indicating that the observed trend in radar echo evolution based on 2-min intervals has some skill in forecasting the future echo intensity on timescales of 10–20 min. However, the data sample presented here is of very limited size and has to be extended for more generalized statements on this subject.

### c. Supercell storm

We applied COTREC to a supercell storm from 15 July 1982, observed with a S-band radar during the hail suppression experiment Grossversuch IV (Federer et al. 1978/79). These radar data have a better spatial resolution than the data discussed up to now. Preprocessing of these data includes a transformation to Cartesian coordinates with a resolution of 0.25 km in space and 1 dB in reflectivity. Animation loops of consecutive radar pictures often show small-scale motion patterns (e.g., rotation) that help to identify the storm type and the internal kinematics of a storm (Houze et al. 1993). The main question here is if COTREC can replicate these features that are best seen visually in animation loops.

COTREC was applied to these data with a time lag of 2 min, a box size of 4 km, and a grid size of 2 km. Figure 8a shows the radar patterns, the COTREC motion vectors, and the patterns of echo growth and decay. Major echo growth is found in the north of the main center of the storm, whereas echo decay occurs in the southern part of the storm. Since the vectors indicate motion from southwest to northeast (while the storm propagated from south-southwest to north-northwest), one can state that the storm is propagating toward the

left side of the motion of the small-scale radar patterns. Plotting the storm-relative instead of the ground-relative motion vectors (see Fig. 8b) shows echoes in the north moving toward the main center of the storm. Our interpretation is that this storm is left-moving and is fed by warm moist air from the north. Cyclonic vorticity is indicated from the motion vectors in the center of the storm. Animation loops of the radar pictures of this storm show cyclonic rotation that is consistent to the COTREC analysis presented here.

## 5. Discussion and outlook

### a. Sensitivity analysis

The type of precipitation, the time lag between two radar pictures, the grid size of the radar data, the grid size of the motion vectors, and the lower threshold of the considered reflectivities are parameters that influence the performance of TREC and COTREC. The optimal choice for a given precipitation depends on the resolution of the data, the type of radar patterns, and the application. For instance, a short time lag is needed in fast evolving situations, but a longer time lag reduces the quantisation error. However, for a longer time lag a larger search area has to be selected. A larger search area means a higher probability that two boxes define by chance an erroneous TREC vector. This probability is also increased by random variations, both in intensity and shape of the radar patterns. Hence, longer time lags lead to more chaotic patterns of echo motion. Rinehart (1981) recommended using a time lag less than 5 min for evaluation of the radar data with the TREC method. Increasing the box size, on the other hand, causes smoothing effects, whereas too small box sizes may increase the rate of erroneous TREC vectors. Rinehart (1981) recommended box sizes of 5–15 km for obtaining optimal results.

In the examples discussed in sections 3 and 4, we used a time lag of 2 min and box sizes and grid sizes for the motion vectors of 4–16 km. To illustrate the influence of these parameters on (CO)TREC, the experiments summarized in Table 2 were performed. The RRMS error between the radial components of the (CO)TREC vectors and the Doppler velocities was

used as a test criterion to answer the following three questions: What is the performance 1) in different precipitation situations, 2) for different time lags, and 3) for different resolutions of the radar data?

### 1) DIFFERENT PRECIPITATION SITUATIONS

The RRMS error was calculated for the precipitation events discussed in sections 3, 4a, and 4b, and the results are given in Table 2. The smaller values of the RRMS error for TREC in the events 2 and 3 (compared to event 1) are caused by the lack of widespread (i.e., purely nonconvective) precipitation. COTREC always yields a smaller RRMS error than TREC for a time lag of 2 min on the order of  $3.5 \text{ m s}^{-1}$ . This strong reduction in all situations means that COTREC can be applied to a wide spectrum of precipitation types.

### 2) TIME LAG

The RRMS error computed with a time lag of 2 min are smaller for all three events than for a time lag of 10 min. This probably reflects the difficulty of (CO)TREC to follow precipitation with a longer time lag. On the other hand, motion vectors based on a long time lag are principally more stable than those based on a short time lag. As a compromise, a time interval of 5 min for computing motion vectors may be optimal for nowcasting purposes. Another possible way to mitigate the weakness of (CO)TREC for time intervals of 10 min may be to repeat the technique several times (e.g., five 2-min steps for a 10-min lag) and then take an average of the individual vectors for extrapolation into the future. Such a procedure might have relevance for nowcasting but needs to be verified.

### 3) RESOLUTION OF THE RADAR DATA

Lowering the size of the radar pixels from 1 to 0.5 km enhances the resolution of the resulting TREC vectors by a factor of 2 in velocity (i.e., from 8.3 to  $4.2 \text{ m s}^{-1}$  when a time lag of 2 min is used). This was applied to event 1 (last line in Table 2). The RRMS error becomes smaller for TREC and somewhat larger for COTREC (compared to 1-km resolution). The

TABLE 2. Comparison of RRMS for different precipitation events: W—widespread (nonconvective) precipitation, C—convective precipitation, DC—deep convective precipitation (1540 UTC 21 July 1992), and H—high-resolution radar data (0.5 km).

Event	Described in	Precipitation type	RRMS TREC	RRMS COTREC
1	Section 3	W/C	10.6 (2 min)	3.6 (2 min)
2	Section 4a	C	5.6 (2 min)	3.3 (2 min)
3	Section 4b	DC	4.9 (2 min)	3.3 (2 min)
1	Section 3	W/C	17.9 (10 min)	12.1 (10 min)
2	Section 4a	C	12.1 (10 min)	9.2 (10 min)
3	Section 4b	DC	6.2 (10 min)	3.7 (10 min)
1	Section 3	W/C	8.2 (2 min, H)	4.3 (2 min, H)

scatter diagrams (not shown here) suggest that these differences are mainly caused by the "widespread" part of the precipitation. The net reduction of RRMS after application of COTREC remains large. Apparently there is an optimum resolution for (CO)TREC. This point requires further investigation.

#### *b. Clutter and shielding*

Section 4a showed that clutter and shielding may cause a retardation effect on the velocities of the COTREC vectors. The main reason for this is that clutter echoes have zero velocity. The procedure in section 2b eliminates part of this influence. But the resulting COTREC vectors may still be contaminated by stationary radar patterns of clutter and shielding. Two ways may help to further minimize this contamination: 1) by applying (CO)TREC to clutter-free regions only, and 2) by preprocessing the radar data in such a way that the stationary patterns of clutter and shielding are eliminated. A sophisticated correction scheme, taking into account the vertical profiles of radar reflectivity, is planned to be used in the new network of three radar stations presently being installed by the Swiss Meteorological Institute in Switzerland (Joss and Lee 1993).

#### *c. Nowcasting*

COTREC may help to search for growth and decay in precipitation, a major cause of poor forecasting when linear extrapolation schemes are used (Browning et al. 1982). COTREC is able to anticipate the patterns of echo growth and decay up to about 20 min in advance in case of severe convective storms. In case of orographic precipitation, the lead time for useful forecasts may be longer when the stationarity of the growth-decay patterns persists and is detected in time. Thus, two apparent motions are important: the motions of the radar echoes and the motions of the growth-decay patterns. The two motions should be extrapolated separately for nowcasting, and this is presently tested with a large sample of radar data (Li and Schmid 1994). If a Doppler radar is available, the comparison between COTREC- and Doppler-derived speeds may allow to distinguish between translating and propagating echoes, an additional criterion for judging the echo evolution for nowcasting. Future research will have to quantify the gain. The scanning strategy (at least one PPI every 2–5 min.) needed for successful application of COTREC fits the requirement for other applications reasonably well. For instance, the future weather radar generation of the Swiss Meteorological Institute (Joss and Lee 1993) will use volume scans (20 PPIs) every 5 min, which would be suitable for COTREC. We plan to develop COTREC further for operational application.

## 6. Conclusions

A method for obtaining the motion, growth, and decay of radar echoes is presented. This method, called COTREC, is an extension of TREC and uses the two-dimensional continuity equation as a strong constraint in the cost function to be minimized. The behavior of this method has been investigated with real radar data.

Comparisons of TREC- and COTREC-derived motion vectors with Doppler data have shown that COTREC reduces the differences between the radial component of the TREC-derived vectors and Doppler velocities. This is obtained by eliminating erroneous TREC vectors (caused by clutter, shielding, and rapid morphological changes of the radar patterns). On average, the RRMS error is reduced from 7 to 3.5 m s<sup>-1</sup> when the time lag is 2 min (see Table 2).

This reduction of errors enhances the chance to detect systematic differences between radial COTREC velocities and Doppler velocities. Propagating precipitation echoes (e.g., caused by sedimentation effects or by orographic growth of precipitation), clutter, and shielding caused by orography are possible reasons for these systematic deviations. A comparison of COTREC and Doppler velocities opens a unique possibility for obtaining quantitative information on the propagating contribution of precipitation echoes, for example, in the cases of orographic precipitation or in severe convective storms.

COTREC can predict the patterns of echo growth and decay in orographic precipitation and in convective storms up to about 20 min in advance. This finding is consistent to the characteristic lifetime (30–45 min) of convective cells. In frontal and orographic precipitation, we hope to extend the predictive performance of COTREC over longer time periods. A larger dataset will help to verify our tentative conclusion: that the best results for nowcasting are obtained when extrapolating separately the apparent motion of the radar echoes and the apparent motion of the growth-decay patterns.

COTREC may also become a tool for the visualization and analysis of the evolution of radar patterns in real time. The computer time needed is negligible (COTREC, implemented on a VAX 9000-420 and on Sun workstations, needs about 20 s of CPU time for the analysis of one sample of radar data). Thus, application of COTREC is attractive for research and holds good promise for operational nowcasting over complex orography.

*Acknowledgments.* We appreciate the generous support of A. Waldvogel. We are also grateful to H. H. Schiesser for carefully drawing part of the figures. We would like to thank R. Rinehart and an anonymous reviewer who greatly helped with their critical comments to improve this paper.

## REFERENCES

- Barclay, P. A., and K. E. Wilk, 1970: Severe thunderstorm radar echo motion and related weather events hazardous to aviation operations. ESSA Tech. Memo. ERLTM-NSSL 46, 63 pp.
- Bellon, A., and G. L. Austin, 1978: The evaluation of two years of real time operation of a short term precipitation forecasting procedure (SHARP). *J. Appl. Meteor.*, **17**, 1778–1787.
- Bergeron, T., 1965: On the low-level redistribution of atmospheric water caused by orography. *Suppl. Proc. Int. Conf. Cloud Phys.*, Tokyo, 96–100.
- Bertsekas, D. P., 1982: *Constrained Optimization and Lagrange Multiplier Methods*. Academic Press, 395 pp.
- Browning, K. A., C. G. Collier, P. R. Larke, P. Menmuir, G. A. Monk, and R. G. Owens, 1982: On the forecasting of frontal rain using a weather radar network. *Mon. Wea. Rev.*, **110**, 534–552.
- Chen, C. S., W. S. Chen, and Z. S. Deng, 1991: A study of a mountain-generated precipitation system in northern Taiwan during TAMEX IOP 8. *Mon. Wea. Rev.*, **119**, 2574–2606.
- Collier, C. G., 1989: *Application of Weather Radar Systems: A Guide to Uses of Radar Data in Meteorology and Hydrology*. Ellis Horwood Limited, 294 pp.
- Federer, B., A. Waldvogel, W. Schmid, F. Hampel, E. Rosini, D. Vento, P. Admirat, and J. F. Mezeix, 1978/79: Grossversuch IV: Design of a randomized hail suppression experiment using the Soviet method. *Pure Appl. Geophys.*, **117**, 548–571.
- Hill, F., K. A. Browning, and M. J. Bader, 1981: Radar and rain gauge observations of orographic rain over south Wales. *Quart. J. Roy. Meteor. Soc.*, **107**, 643–670.
- Hilst, G. R., and J. A. Russo, 1960: An objective extrapolation technique for semiconservative fields with an application to radar patterns. Tech. Memo. 3, The Travellers Weather Research Center, Hartford, CT, 34 pp.
- Houze, R. A. Jr., W. Schmid, R. G. Fovell, and H.-H. Schiesser, 1993: Hailstorms in Switzerland: Left movers, right movers, and false hooks. *Mon. Wea. Rev.*, **121**, 3345–3370.
- Howes, S., 1988: Use of satellite and radar images in operational precipitation nowcasting. *J. Brit. Interplan. Soc.*, **41**, 455–460.
- Joss, J., and A. Waldvogel, 1990: Precipitation measurement and hydrology. *Radar in Meteorology*, D. Atlas, Ed., Amer. Meteor. Soc., 577–606.
- , and A. Pittini, 1991: Real-time estimation of the vertical profile of radar reflectivity to improve the measurement of precipitation in an alpine region. *J. Meteor. Atmos. Phys.*, **47**, 61–72.
- , and R. W. Lee, 1993: Scan strategy, clutter suppression calibration, and vertical profile corrections. Preprints, *26th Conf. Radar Meteor.*, Norman, OK, Amer. Meteor. Soc., 875–878.
- Li, L., 1994: On the use of variational analysis for determining the motion, growth and decay of radar echoes in orographically complex regions. thesis, ETH Zurich, 96 pp.
- , and W. Schmid, 1994: An investigation on the growth and decay of radar echoes in alpine regions. Preprints, *23rd Int. Conf. on Alpine Meteor.*, Lindau, Germany, 56–59.
- Mosimann, L. R., 1994: Die Bestimmung der Verreifung von Schneekristallen mittels vertikalem Dopplerradar. thesis Nr. 10510, ETH Zurich, 99 pp.
- Navon, I. M., and M. L. David, 1987: Conjugate-gradient method for large scale minimization in meteorology. *Mon. Wea. Rev.*, **115**, 1479–1502.
- Passarelli, R. E., Jr., 1981: Autocorrelation techniques for ground clutter rejection. Preprints, *20th Conf. Radar Meteor.*, Boston, MA, Amer. Meteor. Soc., 308–313.
- Press, W. H., B. P. Flannery, S. A. Teukolsky, and W. T. Vetterling, 1991: *Numerical Recipes: The Art of Scientific Computing*. Cambridge University Press, 702 pp.
- Rinehart, R. E., 1981: A pattern recognition technique for use with conventional weather radar to determine internal storm motions. Recent Progress in Radar Meteorology. *Atmos. Technol.*, **119**–134.
- , 1991: *Radar for Meteorologists*. University of North Dakota, 334 pp.
- , and E. T. Garvey, 1978: Three-dimensional storm motion detection by conventional weather radar. *Nature*, **273**, 287–289.
- Sasaki, Y., 1958: An objective analysis based on the variational method. *J. Meteor. Soc. of Japan, Ser. 2*, **36**, 77–88.
- , 1970a: Some basic formalisms in numerical variational analysis. *Mon. Wea. Rev.*, **98**, 875–883.
- , 1970b: Numerical variational analysis formulated under the constraints determined by longwave equations and lowpass filter. *Mon. Wea. Rev.*, **98**, 884–898.
- Schmid, W., 1992a: The prediction of hail. Part I: Radar quantities of hail intensity. *Atmos. Res.*, **28**, 49–69.
- , 1992b: The prediction of hail. Part II: The movement of hail cells. *Atmos. Res.*, **28**, 71–91.
- , D. Högl, A. Vckovski, and J. Joss, 1991: Test of clutter suppression techniques in the Swiss Alps. Preprints, *25th Conf. Radar Meteor.*, Paris, France, Amer. Meteor. Soc., 875–878.
- Sherman, C. A., 1978: A mass-conservation model for wind fields over complex terrain. *J. Appl. Meteor.*, **17**, 312–319.
- Smythe, G. R., and D. S. Zrnić, 1983: Correlation analysis of Doppler radar data and retrieval of the horizontal wind. *J. Climate Appl. Meteor.*, **22**, 297–311.
- Staehelin, J., A. Waldvogel, J. L. Collett, Jr., R. Dixon, W. Henrich, B. Oberholzer, L. Mosimann, A. Prevot, W. Schmid, T. Schumann, M. Steiner, M. Volken, L. Li, and B. Zinder, 1993: Scientific goals and experiments of the projects “winter precipitation at Mount Rigi”: An overview. *Water, Air and Soil Poll.*, **68**, 1–14.
- Tsonis, A. A., and G. L. Austin, 1981: An evaluation of extrapolation techniques for the short-term prediction of rain amounts. *Atmos.-Ocean*, **19**, 54–65.
- Tuttle, J. D., and G. B. Foote, 1990: Determination of boundary layer airflow from a single Doppler radar. *J. Atmos. Oceanic Technol.*, **7**, 218–232.
- Watanabe, H., and Y. Ogura, 1987: Effects of orographically forced upstream lifting on mesoscale heavy precipitation: A case study. *J. Atmos. Sci.*, **44**, 661–675.
- Winston, H. A., and L. J. Ruthi, 1986: Evaluation of RADAP II severe-storm detection algorithms. *Bull. Amer. Meteor. Soc.*, **67**, 145–150.